



HAL
open science

Passive monitoring of a sea dike during a tidal cycle using sea waves as a seismic noise source

Anaëlle Joubert, Mathieu Le Feuvre, Philippe Cote

► To cite this version:

Anaëlle Joubert, Mathieu Le Feuvre, Philippe Cote. Passive monitoring of a sea dike during a tidal cycle using sea waves as a seismic noise source. *Geophysical Journal International*, 2018, 214 (2), pp.1364-1378. 10.1093/gji/ggy180 . hal-03239883

HAL Id: hal-03239883

<https://hal.science/hal-03239883>

Submitted on 27 May 2021

HAL is a multi-disciplinary open access archive for the deposit and dissemination of scientific research documents, whether they are published or not. The documents may come from teaching and research institutions in France or abroad, or from public or private research centers.

L'archive ouverte pluridisciplinaire **HAL**, est destinée au dépôt et à la diffusion de documents scientifiques de niveau recherche, publiés ou non, émanant des établissements d'enseignement et de recherche français ou étrangers, des laboratoires publics ou privés.

Passive monitoring of a sea dike during a tidal cycle using sea waves as a seismic noise source

Anaëlle Joubert, Mathieu Le Feuvre and Philippe Côte

IFSTTAR, Laboratory for Geophysics and Non Destructive Evaluation, LUNAM University, Bouguenais, CS4 F-44344, France. E-mail: anaelle.joubert@ifsttar.fr

Accepted 2018 May 14. Received 2018 April 25; in original form 2017 June 12

SUMMARY

Over the past decade, ambient seismic noise has been used successfully to monitor various geological objects with high accuracy. Recently, it has been shown that surface seismic waves propagating within a sea dike body can be retrieved from the cross-correlation of ambient seismic noise generated by sea waves. We use sea wave impacts to monitor the response of a sea dike during a tidal cycle using empirical Green's functions. These are obtained either by cross-correlation or deconvolution, from signals recorded by sensors installed linearly on the crest of a dike. Our analysis is based on delay and spectral amplitude measurements performed on reconstructed surface waves propagating along the array. We show that localized variations of velocity and attenuation are correlated with changes in water level as a probable consequence of water infiltration inside the structure. Sea dike monitoring is of critical importance for safety and economic reasons, as internal erosion is generally only detected at late stages by visual observations. The method proposed here may provide a solution for detecting structural weaknesses, monitoring progressive internal erosion and delineating areas of interest for further geotechnical studies, in view to understand the erosion mechanisms involved.

Key words: Seismic noise; Seismic interferometry; Seismic attenuation; Surface waves.

1 INTRODUCTION

Seismic surface waves are increasingly used for imaging and monitoring purposes (e.g. Brenguier *et al.* 2008; Duputel *et al.* 2009; Mainsant *et al.* 2012), in particular because they are easily retrieved from seismic interferometry due to their higher energy (Woods 1968) and the shallow distribution of noise sources. Seismic interferometry has the objective of retrieving the impulse response of a medium by processing pairs of simultaneous seismic records, either by cross-correlation (Lobkis & Weaver 2001; Wapenaar 2004) or deconvolution (Vasconcelos & Snieder 2007, 2008a).

In the field of seismology, passive seismic methods have undergone spectacular development in recent years, since it has been shown that the cross-correlation of diffuse seismic noise converges towards the Green's function of a medium (Lobkis & Weaver 2001; Weaver & Lobkis 2001; Campillo & Paul 2003; Shapiro & Campillo 2004; Sabra *et al.* 2005; Wapenaar & Fokkema 2006). This approach has led to: (1) the production of high-resolution tomographic maps (Shapiro *et al.* 2005; Roux 2009; Stehly *et al.* 2009) and (2) the monitoring of geological structures, such as volcanic edifice, geological basin or clay landslide, with a precision better than 0.1 per cent in velocity change (Brenguier *et al.* 2008; Meier *et al.* 2010; Mainsant *et al.* 2012). Using seismic noise instead of punctual energetic sources (earthquake and hammer shot)

presents two main advantages: first, continuous monitoring is possible, provided that noise sources are stable enough in space and time; and second, higher sensitivity is expected in terms of seismic property retrieval, since (1) recording over long periods allows increasing the signal-to-noise ratio and (2) multiple ray paths originating from numerous primary and secondary noise sources allow for a finer-spatial sampling of the medium. Regarding temporal resolution, a compromise must be found by taking into account both the kinematics of changes undergone by the medium and the minimum recording duration required to obtain a converged correlation function.

In parallel, at the near-surface scale, surface waves generated by anthropogenic noise sources, such as traffic, have been analysed to obtain dispersion diagrams and infer the mechanical properties of soils (Park & Miller 2008) for civil engineering purposes. Recently, the seismic sounding of a sea dike was demonstrated, using cross-correlations of noise generated when sea waves caused by swell and surf impact on the structure (Le Feuvre *et al.* 2015). From a monitoring point of view, Planès *et al.* (2016,2017) showed that water infiltration inside an earthen levee could be tracked using delay measurements on cross-correlations, respectively, on an experimental and a real site. In both cases, ambient noise was anthropogenic, being related to nearby machine activity or traffic. Here, we propose to monitor the tidal response of a sea dike using sea waves

as natural seismic sources. We use both phase delay and spectral amplitude measurements, in order to infer variations in terms of velocity and attenuation, respectively. To do this, we calculate the empirical Green's functions either by cross-correlation or by deconvolution, and we compare the results between these two methods (see Section 2).

In recent years, protecting populations against floods has become a priority in many countries, as a result of several catastrophic weather events. In France, sea dikes, walls and levees protect 1350 km of coastline, of which only 400 km are currently documented, reflecting a lack of knowledge on their condition (Colas 2007). Furthermore, these structures appear to be very heterogeneous in terms of resistance, having been built at different epochs (more than 2 centuries ago for the oldest ones), using various materials (usually *in situ* soil), different reinforcement structures (clay core, stone or masonry wall), multiple geometries and subject to irregular maintenance (Rode 2012). Dikes and levees can experience two main failure events: (1) over-topping, which can be prevented by raising the structure; (2) breaching, either due to piping, internal erosion or loss of stability due to seepage in the foundation. Breaching represents about 30 per cent of failure events and is difficult to assess before late erosion stages. At present, managers generally rely on visual observations that do not allow detecting internal defects at the early stage of erosion. Geo-electric studies (Johansson & Dahlin 1996; Inazaki & Sakamoto 2005; Fargier *et al.* 2012; Weller *et al.* 2014), acoustic studies (Rittgers *et al.* 2015) and temperature analysis within dikes (Johansson 1991; Beck *et al.* 2010) have proven capable of detecting soaking zones. Although very efficient, temperature studies using optical fibres present two main drawbacks: (1) they have to be set up inside the dike body during its construction and (2) they give more punctual information than other geophysical methods. Geo-electric studies, the most popular in this context, give volumetric information but are insensitive to mechanical properties. Currently, the seismic methods applied to sea dikes are mainly restricted to (Multi-Channel Analysis of Surface Waves) MASW (e.g. Karl *et al.* 2011) to define a 1-D shear velocity profile in depth. Recently, seismic noise has been used for modal analysis and H/V studies on sea dikes and wharfs, in order to delineate areas of varying stiffness (Fontan *et al.* 2016; Vassail *et al.* 2016).

In this study, we demonstrate that sea waves can be used to monitor sea dikes during part of a tidal cycle, potentially allowing the detection of structural weaknesses from the mechanical standpoint, by installing a linear array of sensors at the top of the structure. A previous experiment (Le Feuvre *et al.* 2015) showed that seismic ambient noise contains sufficient energy at relevant frequencies for sounding both the dike body and its substratum, providing recordings lasting several minutes. Carrying on from this work, experiments were conducted on the same study site (Les Moutiers-en-Retz, Pays de la Loire, France), in order to monitor the response of the structure to hydraulic solicitation during a tidal cycle. In the next section, we introduce generalities regarding the analysis of seismic noise and both principles of cross-correlation and deconvolution, and describe the specific approach used in this study to obtain relative variations as a function of time, based on delay and spectral amplitude measurements. We then present the field site on which the experiment was carried out as well as the recording equipment and protocol. The results are given in the last section, wherein are shown relative variations of the surface wave velocity and the attenuation coefficient as a function of time, frequency and location along the structure. The different approaches taken in this study are compared and a physical interpretation of the variations observed is proposed.

2 METHOD

2.1 Cross-correlation or deconvolution calculation

It has been shown that, under the assumption of a diffuse seismic field, the cross-correlation of two seismic ambient noise records can be used to reconstruct the Green's function (filtered impulse response) of a medium (see Lobkis & Weaver 2001; Snieder 2004, 2006; Snieder & Şafak 2006; Wapenaar & Fokkema 2006, for theoretical studies, and Shapiro & Campillo 2004 and Shapiro *et al.* 2005 for practical applications). A diffuse seismic field is produced, either when primary noise sources are equidistributed (at least on an average during the recording time) or when the medium is heterogeneous enough to provide a sufficient number of secondary sources.

However, even in the case of an imperfect reconstruction, the correlation function still contains useful information on the medium, providing that the spatial distribution of the seismic sources does not vary significantly with respect to changes in the physical properties of the medium. Thus, it is possible to track this change over time. Monitoring methods using seismic noise are generally based on surface waves, since these are easily retrieved from cross-correlation. These methods usually benefit from the existence of diffracted surface waves produced by heterogeneities. In such case, measurements of relative velocity changes are performed by accounting for the fact that when the medium undergoes a homogeneous change in velocity, later arrivals present a longer delay than early arrivals due to their greater propagation distance. Two different approaches can be used: the doublet method (Poupinet *et al.* 1984) and the stretching method (Snieder *et al.* 2002; Snieder 2006). Several applications have demonstrated the efficiency of monitoring methods based on seismic noise for tracking volcanic eruptions (Brennguier *et al.* 2008; Duputel *et al.* 2009), monitoring clay landslide failure (Mainsant *et al.* 2012) and monitoring seasonal velocity variations (Meier *et al.* 2010). When the medium is not sufficiently heterogeneous for the existence of strong seismic scattered waves, it is still possible to calculate relative velocity variations exclusively on the direct surface wave, providing that this variation is large enough to compensate for the loss of sensitivity induced by the absence of coda.

Cross-correlations are generally calculated from signals which are beforehand whitened in order to enhance the diffusivity of the seismic field by compensating for the non-flat nature of its spectrum (Bensen *et al.* 2007). The whitened noise record is calculated as

$$\tilde{S} = \frac{S \cdot |S|}{|S|^2 + \epsilon^2}, \quad (1)$$

where S is the Fourier transform of the signal and ϵ is a small number that prevents from equalizing near-zero components of the raw spectrum (Clayton & Wiggins 1976). The empirical Green's function is then obtained by cross-correlation:

$$\gamma_{j,k} = \tilde{S}_j^* \cdot \tilde{S}_k, \quad (2)$$

where j and k are receiver indices and the symbol $*$ stands for the complex conjugate.

While cross-correlation is generally the mathematical operation used for interferometry, deconvolution is an alternate way of reconstructing empirical Green's functions. For example, Snieder (2006) used deconvolution to extract the response of a building during an earthquake, while Mehta *et al.* (2007) used deconvolution to obtain the near-surface propagation matrix from the recording of a teleseismic event in a borehole array. Prieto *et al.* (2011) used a similar approach to calculate the impulse response function of a building

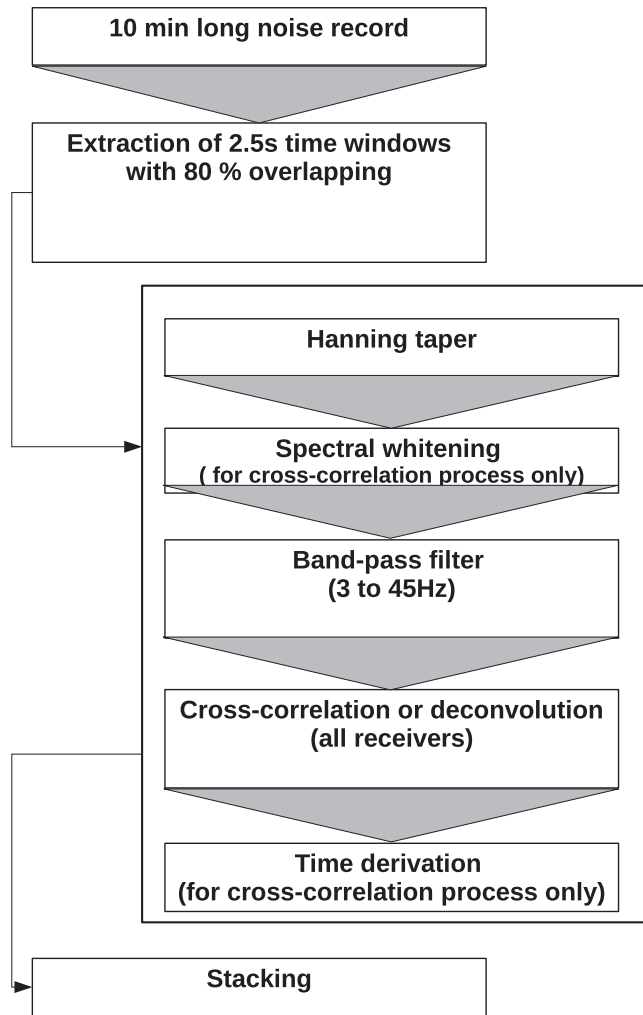


Figure 1. Data processing scheme.

using ambient vibrations. The two operations have been compared in several studies (Vasconcelos & Snieder 2007, 2008a; Bitri *et al.* 2011; Nakata *et al.* 2013). Despite some reports stating that pre-whitened cross-correlations do not allow for the retrieval of true Green's function amplitudes (Weaver & Lobkis 2001; Larose *et al.* 2007), evidence of the opposite effect can be found in a number of studies (Matzel 2007; Cupillard & Capdeville 2010; Cupillard *et al.* 2011). This can be intuitively understood by considering the fact that the propagation medium reduces the amount of coherent signal as a function of distance, because of geometrical spreading, attenuation and scattering. Nevertheless, the retrieval of true Green's function amplitudes seems more dependent on favourable noise conditions, that is, a strictly diffuse noise field, for cross-correlation than for deconvolution (Prieto *et al.* 2011; Nakata *et al.* 2013). This makes the latter the preferred approach for attenuation studies. Regarding the phase information, both cross-correlation and deconvolution seem to be able to produce reliable empirical Green's functions, although deconvolution may introduce spurious arrivals (see Vasconcelos & Snieder 2008a,b for details). In this study, we compare the two approaches in the context of sea dike monitoring.

The empirical Green's function may be calculated by deconvolution as follows:

$$\gamma_{j,k} = \frac{S_k^* \cdot S_j}{(S_k^* \cdot S_k) + \epsilon^2} \quad (3)$$

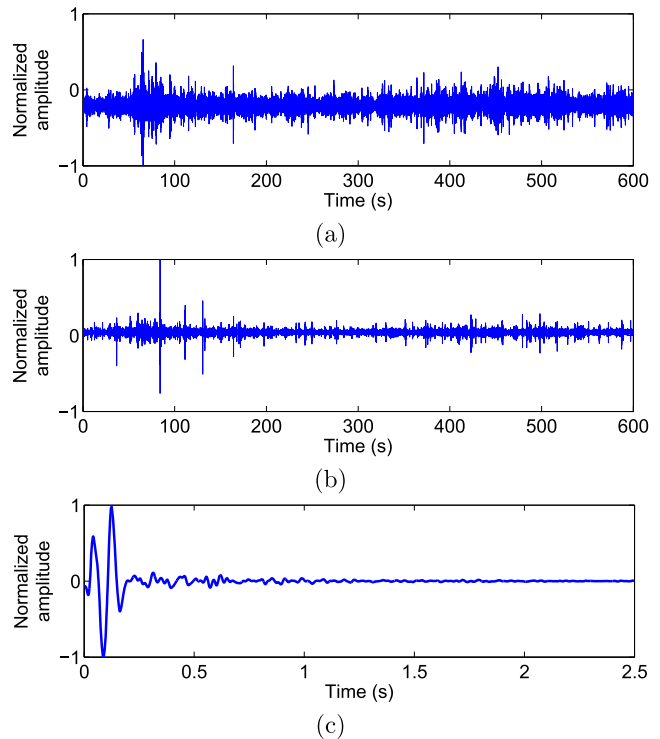


Figure 2. (a and b) Simultaneous records obtained with two sensors 9 m apart at high tide. (c) Result of their cross-correlation after the processing described in Fig. 1

In contrast to the classical cross-correlation approach (see eqs 2 and 5), pre-whitening is not applied.

The processing steps performed in this study to obtain empirical Green's functions are summarized in Fig. 1. Records of 10 min are divided into subrecords of 2.5 s, with an overlap of 80 per cent between subrecords, in order to increase the signal-to-noise ratio of the reconstructed signal (Seats *et al.* 2012). Each subrecord is detrended, tapered with a Hanning window, whitened in the spectral domain (only for cross-correlations, not for deconvolution functions) and then filtered between 3 and 55 Hz. Cross-correlations or deconvolution functions are calculated between subrecords for all possible pairs of sensors, derived in the time domain (only for cross-correlations) and stacked over a 10-min recording period. In order to further increase the signal-to-noise ratio, the causal and anticausal parts of the resulting signal are also summed, after ensuring that both parts show consistent arrivals (Bensen *et al.* 2007). For ideal conditions (i.e. diffuse seismic field), the causal part (i.e. positive time delays) of the empirical Green's function between A and B reproduces the signal that would be recorded in B after an impulse source emits in A. Reciprocally, the anticausal part (i.e. negative time delays) is symmetrical to the causal part and is similar to the time-reversed signal that would be recorded in A after an impulse source emits in B. In practice, summing both parts of an imperfect empirical Green's function allows to mitigate deviations from the ideal conditions (e.g. noise directivity) to some extent (Bensen *et al.* 2007). An example of empirical Green's function is shown in Fig. 2. We choose not to apply any temporal normalization (e.g. clipping or one-bit normalization), which is sometimes used in order to reduce the contaminating effect of transient and localized high-amplitude events, but at the cost of strong distortions of the original records. Instead, we prefer to use short time windows on the raw time series for the same purpose (see Prieto *et al.* 2011).

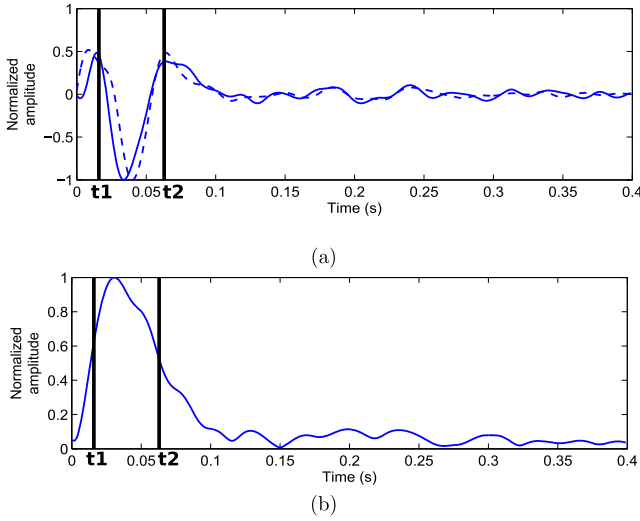


Figure 3. (a) Correlation functions obtained for a given pair of receivers at two different times (full line: first measurement time; dashed line: high tide) showing a phase shift in the surface wave traveltime. (b) Envelope function of the reference signal used to extract the direct surface wave.

The entire set of empirical Green's functions is used to calculate a dispersion diagram, considering that each receiver is a virtual source, and summing each identical distance to increase the signal-to-noise ratio (Gouedard *et al.* 2008; Le Feuvre *et al.* 2015). The dispersion diagram gives a laterally averaged relationship between wavelengths and frequencies, and allows estimating the depths investigated. It is calculated as

$$DD(f, V) = \left| \sum_{j=1}^N \sum_{k=j}^N \text{fft}(\tilde{\gamma}_{j,k}) e^{\frac{i2\pi f d_{j,k}}{V}} \right|, \quad (4)$$

where f is the frequency, V is the phase velocity, N is the number of sensors, $d_{j,k}$ is the distance between sensors j and k and $\tilde{\gamma}_{j,k}$ represents the symmetrical part of the empirical Green's function, where the causal part and anticausal parts are averaged.

2.2 Delay measurement

After applying a Butterworth filter in a given frequency band, direct surface waves of the empirical Green's functions are windowed according to a given amplitude threshold on the signal's envelope. The delay δt is then measured as the time shift corresponding to the maximum value of the cross-correlation between two windowed empirical Green's functions obtained for the same sensor pair at two different times (Fig. 3a):

$$CC(\delta t) = \int_{t_1}^{t_2} \gamma_{j,k}(t + \delta t) \gamma_{j,k}^{ref}(t) dt \quad (5)$$

with t_1 and t_2 being the boundaries of the time window defined by the envelope function (Fig. 3b). The relative phase velocity variation is finally obtained as

$$\frac{\delta v}{V} = -\frac{\delta t}{\frac{(t_1+t_2)}{2}}. \quad (6)$$

This approach was favoured with respect to the stretching method, because the reconstructed signal does not exhibit clearly reproducible coda waves (the non-reproducibility of coda waves is discussed in more details in Section 3.3). Moreover, coda waves are expected to sample a larger volume surrounding a given sensor

pair, and we are here interested in localizing variations of seismic properties along the dike's crest with the best possible accuracy.

In this application, relative velocity variations are calculated with respect to a reference time chosen as the earliest usable measurement, 1 hr and 45 min before the high tide. This time corresponds to the time of contact between the sea and the structure, mandatory to produce suitable seismic noise (see next section).

2.3 Spectral amplitude ratio

The amplitude decay of a circular surface wave can be written as

$$A(f, r) = A_0 \frac{1}{\sqrt{r}} e^{-\alpha(f)r}, \quad (7)$$

where r is the propagation distance from the source, A_0 is the initial amplitude, $\frac{1}{\sqrt{r}}$ accounts for geometrical spreading and α is the attenuation coefficient. The latter can be expressed as (Johnston *et al.* 1979)

$$\alpha(f) = \frac{\pi f}{Q V(f)}, \quad (8)$$

where f is the frequency, Q is the quality factor and $V(f)$ is the surface wave phase velocity. For a given pair of sensors, j and k , the temporal variation of the attenuation coefficient is calculated as

$$\alpha^t(f, x_{j,k}) - \alpha^{ref}(f, x_{j,k}) = \frac{\ln(|F_{j,k}^{ref}(f)|/|F_{j,k}^t(f)|)}{d_{j,k}}, \quad (9)$$

where f is the frequency, $d_{j,k}$ is the distance between sensors j and k , $F_{j,k}^t(f)$ is the Fourier transform of the empirical Green's function at a given time t , $F_{j,k}^{ref}(f)$ is the corresponding value at a chosen reference time and $x_{j,k}$ is the centre of the pair of sensors considered. Eq. (9) measures the temporal variations of the empirical Green's function amplitude spectrum. Like the delay measurement method, the reference chosen is the earliest usable measurement, 1 hr and 45 min before the high tide. The analysis is based on the attenuation coefficient α rather than the quality factor Q , because determining the latter would require estimating the velocity variations first (see eq. 8), thus introducing measurement errors in the results. Since measurements are made directly in the frequency domain, eq. (9) provides a more straightforward relationship with the depth investigated than filtered time functions.

3 EXPERIMENTATION

3.1 Description of site and experiment

The site studied is an earthen sea dike located in Les Moutiers-en-Retz, western France. This structure was built in the 1960s to protect an urban area against flood. The body, about 5 m high and partially sanded, is made of sandy clay and protected by a masonry wall. The basement is composed of sand on top of shales, according to a borehole sounding 500 m away (Fig. 4a).

This sea dike is subject to intense stress by sea waves generated by swell and surf during the tidal cycle. Consequently, some parts of the structure present clear erosion marks, such as bulges (probably caused by hydraulic pressure inside the dike body) and masonry disjoining. Furthermore, a water leak can be observed at the base of the structure when the sea retreats. The masonry is regularly repaired and has been reinforced with shotcrete many times. We chose to monitor the most damaged section of the dike, by installing twenty four 4.5 Hz vertical geophones spaced 3 m apart on

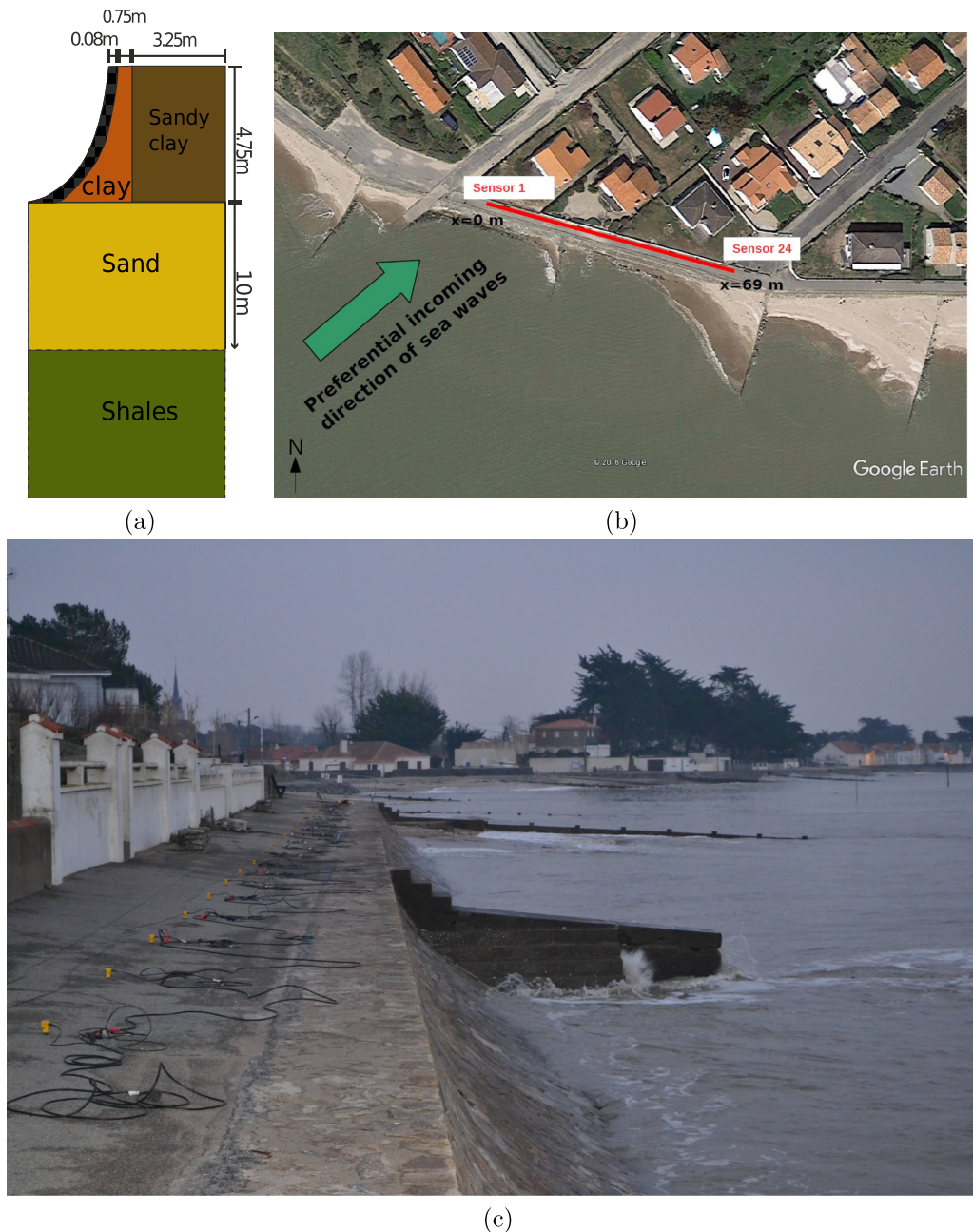


Figure 4. (a) Layout of the dike structure. (b) Field area and array geometry. 24 vertical geophones, with natural frequencies of 4.5 Hz, were installed on top of a sea dike spaced 3 m apart. (c) Photograph of the experiment.

the crest (a view of the array layout and a photograph of the dike during the experiment are shown in Figs 4(b) and (c), respectively). Ambient noise was recorded on 2015 May 18, for 3 hr and 30 min, while the sea was in contact with the structure. Pedestrian traffic was interrupted to ensure that the noise recorded came mainly from the sea waves. Sea level changes are mandatory in order to observe the effect of intruding water during a tidal cycle, and sea wave energy must be sufficient to generate reliable empirical Green's functions. Both these pre-requisites are governed by the tidal coefficient, wind direction and atmospheric pressure. The results given below were obtained for a tidal coefficient of 102, a wind with a southwest direction and speed of 11 km h^{-1} (gusts at 31 km h^{-1}), and an atmospheric pressure of 1012 hPa (source: <http://meteociel.fr>). Fig. 5

shows multiple seismic sea wave impacts propagating within the dike body.

We compare seismic noise spectra at high and low tides to confirm that the seismic noise recorded was generated by sea wave impacts. As can be seen in Fig. 6, the amplitude of the seismic noise increases by a factor of about 10 between 10 and 60 Hz as the sea level rises. Moreover, this higher amplitude corresponds to a coherent surface wave propagation mode, as observed after calculating a dispersion diagram on the cross-correlated signals with eq. (4) (Fig. 7). This dispersion diagram also demonstrates that the frequency content of seismic noise is suitable for sounding both the dike body and its substratum: the dispersion mode reaches a plateau above 20 Hz, corresponding to a relatively homogeneous dike body

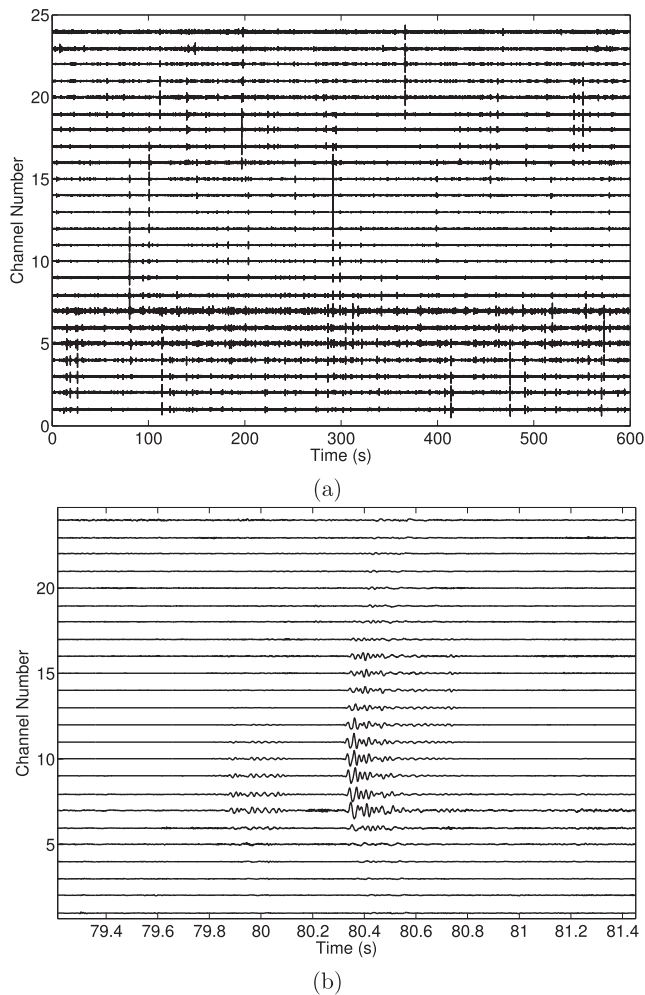


Figure 5. (a) Passive data recorded for 10 min at high tide. (b) Zoom showing individual impacts of sea waves.

with a velocity of 340 m s^{-1} ; below 20 Hz, that is, for wavelengths larger than 17 m, the velocity increases as the surface waves reach the substratum. We note that a mixing between the fundamental and higher mode is possibly observed above 20 Hz. Some contribution from the acoustic wave is also possible at this velocity.

In order to obtain a velocity model as a function of depth, we invert this dispersion mode using the neighbourhood algorithm (Wathelet 2008), under the assumption of a semi-infinite stratified soil, neglecting in particular any potential effect induced by the 3-D geometry of the dike. The result of the inversion is given in Fig. 8 for a three-layer parametrization, showing the first layer with a thickness of about 4.75 m and a shear velocity of about 340 m s^{-1} , which is interpreted as the dike body. The second layer extends up to 15 m in depth, with a shear velocity of about 400 m s^{-1} and is identified as the sand basement. The deepest layer, with a velocity of about 800 m s^{-1} , corresponds to the shale formation.

3.2 Numerical analysis of delay measurements

In order to assess the accuracy of relative velocity variation estimates from delay measurements, we simulate the propagation of surface waves in a simplified version of our field experiment. We use a modified version of the reflection/transmission coefficients method (Kennett 1974; Hisada 1995; Lai & Rix 1998) to calculate

the vertical displacement of Rayleigh waves generated by a vertical point-force source in a stratified medium. The velocity profile of the model is taken according to inversion results described in the above section. The source is located at $x = 0 \text{ m}$ and 24 sensors are arranged with a spacing of 3 m, the first one being located at 3 m from the source. We assume that our real experiment provides empirical Green's functions that are close enough to the surface wave component of the exact Green's function of the medium, and that the synthetic signal recorded at X metres from the source is identical to the empirical Green's function obtained from a pair of sensor located X metres apart. We further neglect any potential effect related to the 3-D structure of the sea dike. Compressional velocities are chosen by setting the Poisson coefficient equal to 0.25 and all densities are set to 2000 kg m^{-3} . We run two simulations, one with the above medium and a second with a modified version of the model, where the shear velocity of the first layer is decreased by 10 per cent. We calculate relative velocity variations with the exact same parameters as for our real experiment: surface waves are filtered in two different frequency bands (Gaussian filter with central frequencies f_c of 10 and 30 Hz, and a standard deviation of $0.3 f_c$ in order to distinguish between variations occurring only within the dike body and deeper variations) and windowed according to a threshold value measured on the envelope of the reference signal (corresponding here to the first model).

The relative velocity variations are presented in Figs 9(a) and (b) as a function of sensor spacing, respectively, for the low- and high-frequency signals. It is seen that short offsets does not allow for unbiased measurements, whereas a plateau is reached at large offsets. The plateau value depends on the central wavelength of the filtered signals because of the sensitivity of the surface wave in depth. The maximum observable wavelengths between two sensors is likely related to a combination of spatial sampling (i.e. sensor spacing) and near-source effects, it also depends on the velocity profile of this particular medium and the depth at which variations occur. We do not attempt to give a specific rule of thumb for sensor spacing as a function of targeted wavelength, but rather use the values obtained from this numerical simulation. Real measurements will be interpreted only for sensor spacings larger than 9 m at high frequencies (21–39 Hz) and 15 m at low frequencies (7–13 Hz), corresponding to respective central wavelengths of 11 and 55 m.

3.3 Data evaluation

Passive monitoring studies require careful choice of the recording window from which individual empirical Green's functions are calculated. Longer time windows provide better signal reconstruction by statistical averaging of noise sources, while shorter time windows provide more precise follow-up of the dynamical processes at work. We perform a convergence test as a function of recording time, with a reference correlation function obtained from a 10-min time window, for different distances between the sensors and within two frequency bandwidths (7–13 Hz and 21–39 Hz). The similarity between waveforms was measured with the calculation of a correlation coefficient. As shown in Fig. 10(a), convergence is achieved within a few minutes at low frequencies, regardless of the distance between the sensors. At higher frequencies (Fig. 10b), convergence is slower because of attenuation, and is not perfectly achieved within 10 min for distances longer than 30 m. Nonetheless, we chose to calculate individual empirical Green's functions with 10-min time windows, in order to closely monitor changes in the water level. It

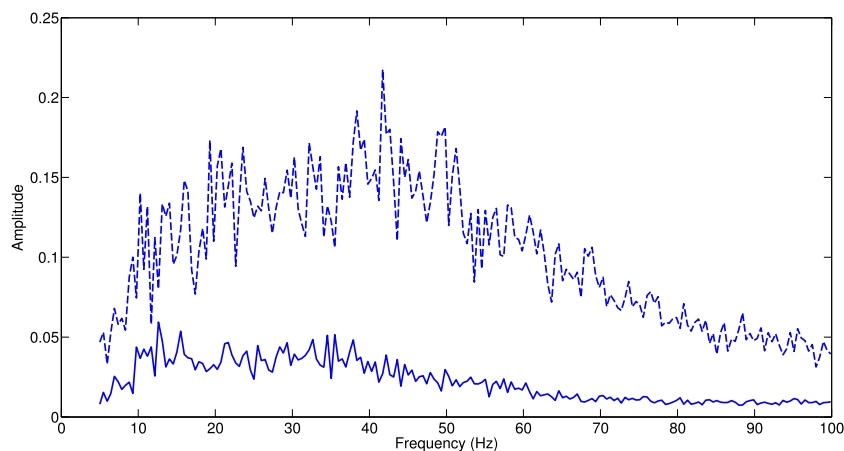


Figure 6. Raw noise data amplitude spectra at high tide (the dashed line) and before contact between the sea and the structure (the full line).

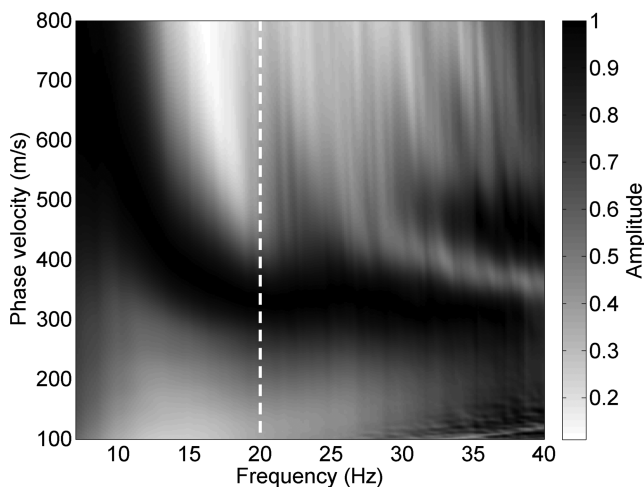


Figure 7. Dispersion diagram obtained from all the calculated correlation functions. The white dashed vertical line marks the lowest frequency for the sounding of the sea dike body only.

should be noted that the results for distances longer than 30 m must be interpreted with caution.

The exact reconstruction of the Green's function is not mandatory for our analysis, since it is based on relative measurements. Even so, noise sources must remain spatially stable to prevent bias in the temporal variation measurements. Fig. 11 represents the cross-correlation obtained at high tide, sorted and stacked as a function of the offset between receivers. It can be seen that the causal and anticausal parts are almost symmetrical in terms of arrival time, implying that the source distribution is close to uniform distribution. In this particular context, the diffusivity of the noise field comes from the multiplicity of primary noise sources rather than from scattered waves induced by heterogeneities. Nevertheless, this constitutes on average a diffuse wavefield (providing that the record window is long enough), which allows for a good reconstruction of empirical Green's functions. This point has been addressed in more details in Le Feuvre *et al.* (2015), where it is shown that a parallel distribution of discrete primary noise sources is suitable for the reconstruction of surface waves.

Fig. 12 gathers successive empirical Green's functions as a function of time, calculated between sensors located at $x = 45$ m and $x = 63$ m. In this example, a clear and gradual phase shift is seen

on the direct surface wave train, while we do not observe a reproducible coda wave. The absence of consistent scattered waves could possibly be explained by the fact that, due to the bad condition of the dike, the medium changes too quickly, inducing strong variations of the coda between two consecutive measurements and making the waveform comparison impractical. More likely, late arrivals could be inconsistent artefacts due to an imperfect reconstruction rather than scattering. Scattering is indeed expected to be weak, because of the small average dimension of heterogeneities compared to the wavelengths of interest (minimum wavelength is about 7 m, while no heterogeneities larger than 1 m are expected).

To ensure that the source distribution does not vary in space during the experiment, we performed plane-wave beamforming (Rost & Thomas 2002) as a function of the azimuthal noise direction at different times. At a given test location, the beamforming output is obtained by integrating the dispersion diagram over frequencies and velocities (see Le Feuvre *et al.* 2015 for more details). As can be seen in Fig. 7, the beamforming output is calculated for velocities ranging from 100 to 800 m s^{-1} and for two different frequency bands (7–13 Hz and 21–39 Hz). Fig. 13 compares the beamforming output for a 1 hr and 45 min time interval, between the first measurement and high tide. It is noteworthy that low-frequency noise originates mainly from the west of the array (in agreement with the fact that unnormalized anticausal parts of the correlation functions exhibit larger amplitudes than their causal counterparts), while higher frequency noise is more homogeneously distributed. This can be explained by the fact that the low-frequency noise corresponds to distant sea impacts, mainly located on the dike bend at the west of the array (see Figs 4b and c), whereas high-frequency noise corresponds to sea wave impacts in front of the dike, on the masonry wall. For these two frequency bands, the spatial repartition of seismic noise sources doesn't vary significantly between the first measurement and the high tide measurement. We consider that it is stable during our experiment.

4 RESULTS AND DISCUSSION

In this section, changes experienced by the medium will be given both in terms of velocity and attenuation variations, as a function of time and sea level.

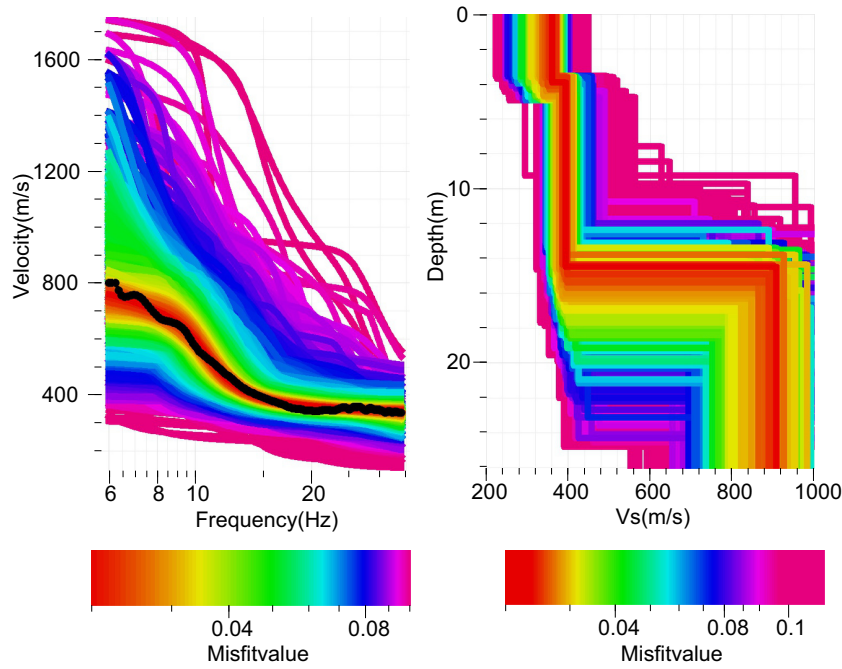


Figure 8. Dispersion curve inversion. Left: measured fundamental mode (in black) compared with the set of analytical modes calculated for all the investigated models (coloured lines). Right: shear velocity models as a function of depth. The best velocity profiles correspond to low misfit values. Inversion is performed with the Dinver software (M. Whatelet, <http://geopsy.org>).

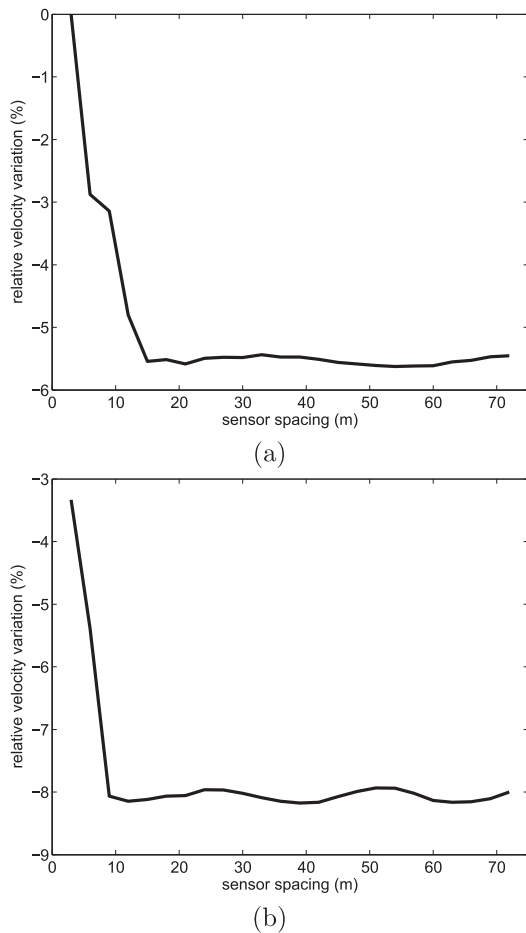


Figure 9. Numerical results for delay measurements. Relative velocity calculation as a function of sensor spacing, (a) for 10 Hz central frequency and (b) 30 Hz central frequency.

4.1 Relative velocity variations

We calculated the relative velocity variations with eq. (6), using the first measurement (corresponding to the first 10 min of the experiment) as reference. The correlation functions were filtered in two distinct frequency bands: (1) between 7 and 13 Hz, so that the measurement includes both the variations within the dike body and its substratum; (2) between 21 and 39 Hz, in order to restrict the analysis to the dike body only. Results are given as pseudo-section panels, whose x-axis corresponds to the centre of each pair of sensors, and whose y-axis corresponds to the distance between them. Since one set of empirical Green's functions is obtained within a 10-min time window, a temporal series of pseudo-sections is finally obtained. We show in Fig. 14 the panels corresponding only to the high tide measurement.

In Figs 14(a) and (b), relative velocity variations are shown for all available sensor pairs, for the high- and low-frequency bands, respectively. Figs 14(c) and (d) give the maximum value of correlation coefficient calculated for each data point shown in Figs 14(a) and (b), respectively (see eq. 5). Figs 14(e) and (f) only display data points with correlation coefficients better than 0.85, and further exclude the values obtained with sensor spacing smaller than the minimum distance defined with numerical modelling (see Section 3.2). We decided to show data points obtained for sensor spacings larger than 30 m, even if convergence was not perfectly achieved at high frequency (see Section 3.3), as long as the correlation coefficient is better than 0.85.

A large low-velocity area can be observed on the low-frequency panel (Fig. 14b), located between $x = 30$ m and $x = 60$ m. The decrease of velocity between the first measurement and the high tide (1 hr and 30 min later) is of the order of 5 per cent. A smaller area of decreasing velocity is observed at about $x = 20$ m. The panel appears smooth, as a result of the large integrated volume at these low

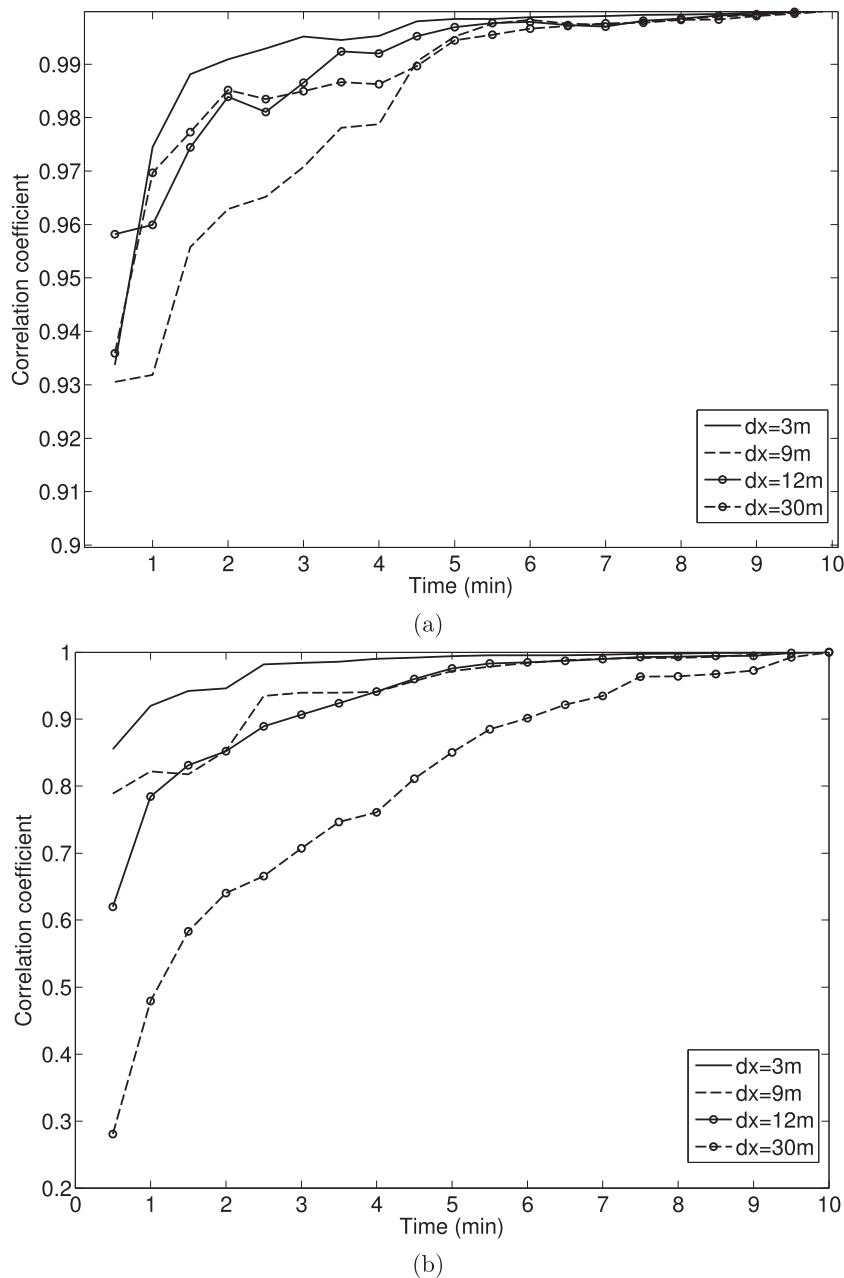


Figure 10. Convergence analysis on correlation functions obtained for different sensor spacings (dx) filtered in two different bandwidths: between 7 and 13 Hz (a) and between 21 and 39 Hz (b).

frequencies, despite the fact that the data points were obtained independently. The high-frequency panel (Fig. 14a) is noisier, which could be related not only to lower signal-to-noise ratios but also to a possible mixing between the fundamental and higher modes (see Fig. 7). Nevertheless, the same large area of decreasing velocity is seen, with a larger amplitude of variation, of the order of 10 per cent. The comparison between the low- and high-frequency results suggests that changes occurred mainly within the dike body, since the amplitude of variation is larger for more superficial depths. We remark that, for the high-frequency results, several data points exhibit a velocity increasing as the sea level rises, in particular between $x = 10$ m and $x = 30$ m along the crest. These data points appear to be associated with low correlation coefficients (Fig. 14c), suggesting that the delay measurement was less accurate in this

area, probably because of waveform changes during the tidal cycle. We note that this area coincides with the location of concrete stairs descending from the masonry wall to the beach and which is submerged at high tide.

Fig. 15 presents temporal variations measured on two different sensor pairs, both located above the area of decreasing velocity observed within the 7–13 Hz and 21–39 Hz frequency limits, respectively, in comparison with the theoretical sea level estimated in the bay (source: <http://shom.fr>). A spacing of 15 m was chosen for the first pair (sensors located at $x = 27$ m and $x = 42$ m), while a spacing of 27 m was chosen for the second pair (sensors located at $x = 27$ m and $x = 54$ m). All the measurements gave the following consistent information:

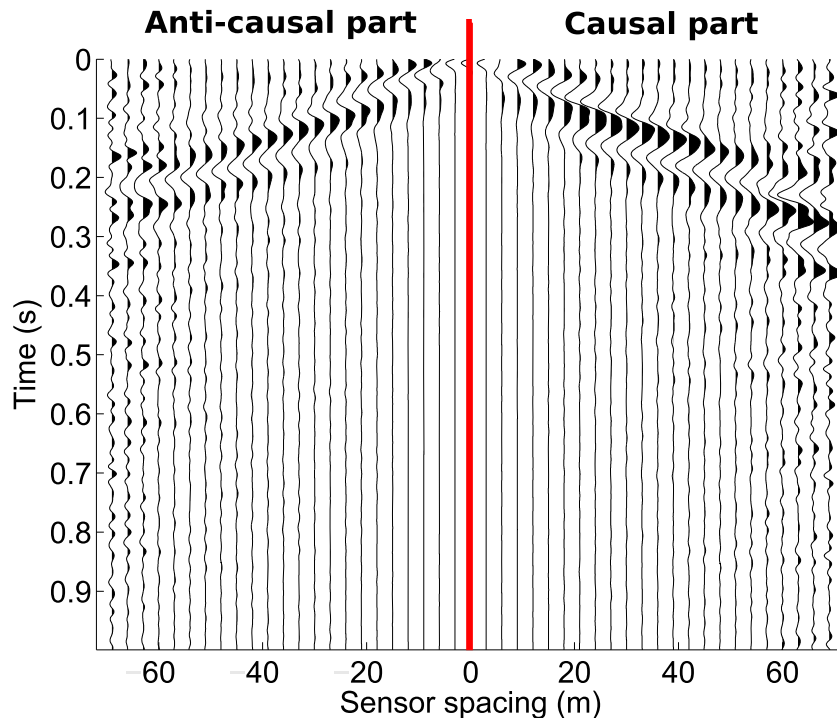


Figure 11. Normalized cross-correlations obtained at high tide, sorted and stacked as a function of the offset between receivers.

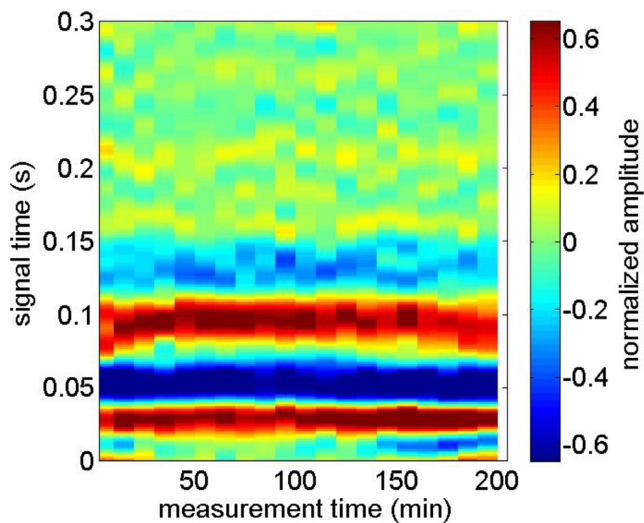


Figure 12. Empirical Green's functions shown as a function of measurement time, obtained from sensors located at $x = 45$ m and $x = 63$ m.

(1) The highest velocity variations were observed on the shortest sensor pair of the high-frequency panel (between 21 and 39 Hz), reaching 10 per cent at high tide. This corresponds to changes in a localized and shallow area within the dike body (central wavelength of about 11 m).

(2) Smaller velocity variations were observed on the longest sensor pair of the high-frequency panel, with a maximum decrease of about 5 per cent, due to the largest lateral averaging. The smallest velocity variations were measured on the low-frequency panel, about 4 and 3 per cent for the short and long sensor pairs, respectively, attributed to the largest volume of investigation in depth.

These results indicate that the variations observed in relation to the tidal cycle were mainly associated with the changes within the sea dike body, rather than its substratum.

We note that very similar results (not shown here), although slightly noisier, were obtained using deconvolution instead of pre-whitened cross-correlation. Cross-correlations without pre-whitening were also tested, with almost identical results at low frequency. At high frequency, the lack of spectral whitening led to very noisy pseudo-sections.

4.2 Attenuation coefficient variations

As we anticipate a strong influence of pre-processing in the retrieval of true amplitudes during the calculation of empirical Green's functions, we compare three different sets of empirical Green's functions, obtained respectively from: (1) no pre-whitening and cross-correlation (eq. 2); (2) pre-whitened cross-correlation (eqs 1 and 2); (3) deconvolution (eq. 3).

Results are calculated for different sensor spacings, in order to investigate the effect of wavelength on resolution. For a given sensor spacing, a series of pseudo-sections is calculated as a function of time. Each pseudo-section corresponds to differences in attenuation coefficient between a given time and the reference time (eq. 9); the x -axis corresponds to the location on the dike's crest, given by the centre of the sensor pairs, and the y -axis, related to depth, corresponds to frequency. Fig. 16 shows attenuation variations calculated at high tide, for sensor spacings of 3, 9 and 12 m, respectively. The reference time is the first measurement of the experiment, 1 hr and 30 min before the high tide.

Fig. 16(a) shows results for non-pre-whitened cross-correlations and a sensor spacing of 3 m. Two distinct areas are observed: (1) an increase of attenuation at high tide, localized between $x = 30$ m and $x = 60$ m, with a difference of about 0.5 m^{-1} with respect to the reference time; (2) a global decreasing of attenuation elsewhere,

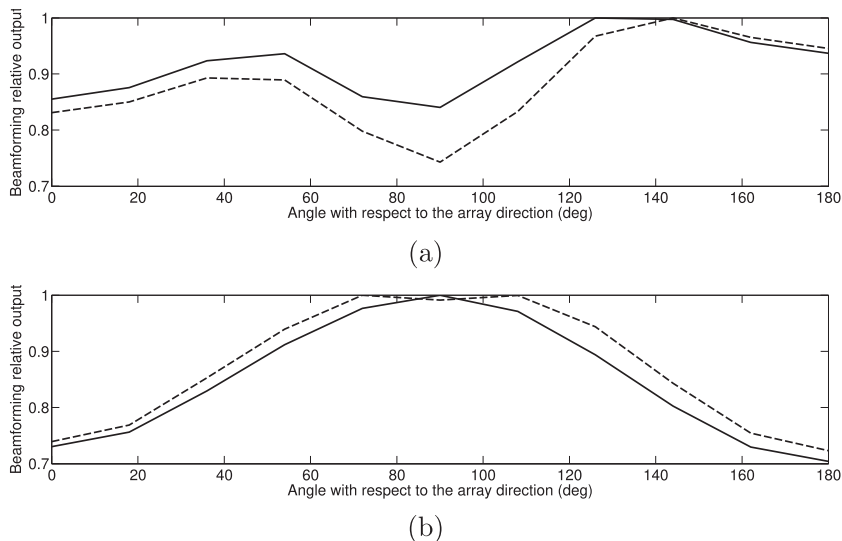


Figure 13. Beamforming relative output obtained with the correlation functions calculated at the time of the first measurement (the full line) and at high tide (the dashed line) for two different bandwidths: between 7 and 13 Hz (a) and between 21 and 39 Hz (b).

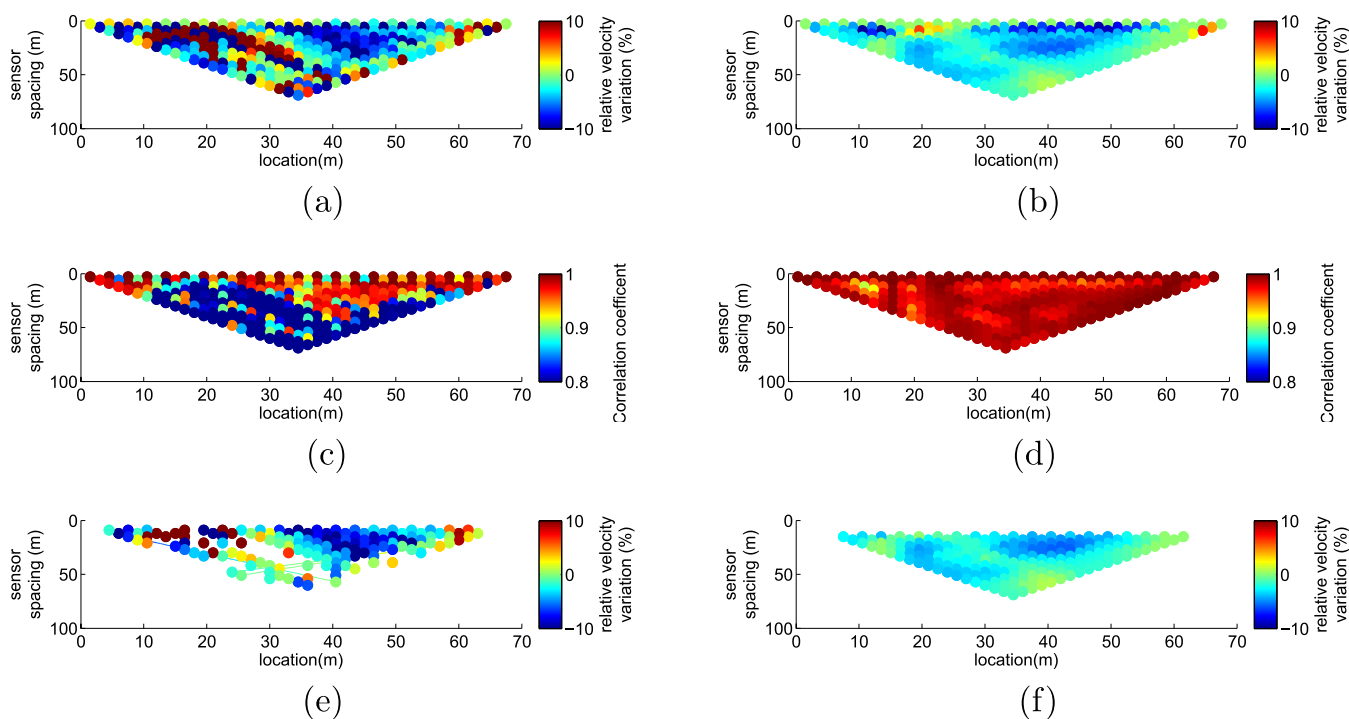


Figure 14. Relative velocity variations obtained at high tide, using the time of the first measurement as reference. The x -axis corresponds to the centre of the sensor pair used for the calculation and the y -axis corresponds to the sensor spacing. Left column: results filtered between 21 and 39 Hz; right column: results filtered between 7 and 13 Hz. (a and b) relative velocity variations; (c and d) correlation coefficients; (e and f) relative velocity variations with correlation coefficient larger than 0.85.

with a change of about 0.5 m^{-1} . The location of the increasing attenuation area is consistent with the largest and strongest area of velocity decreasing seen in Fig. 14, also located between $x = 30 \text{ m}$ and $x = 50 \text{ m}$. Results appear relatively unconstrained in terms of frequency, probably because the sensor spacing is small compared to the wavelengths of interest (see Section 3.2); for example, the wavelength is 11 m at the base of the dike. Nevertheless, maximum variations are seen between 25 and 40 Hz, which corresponds to the dike body. The surrounding medium exhibits a global decreasing of attenuation when the sea level rises. We interpret this effect as a

bias induced by the increasing energy of sources (sea waves) when the tide comes in.

Fig. 17 shows the temporal evolution of the seismic noise energy in comparison with attenuation variations calculated between sensors located at $x = 0 \text{ m}$ and $x = 12 \text{ m}$. It is seen that the noise energy increases as the sea level rises, and that the global attenuation variation seen in Fig. 16(a) is strongly correlated with noise energy. Because no pre-whitening was applied, source energy variations are not compensated. This global decreasing of attenuation

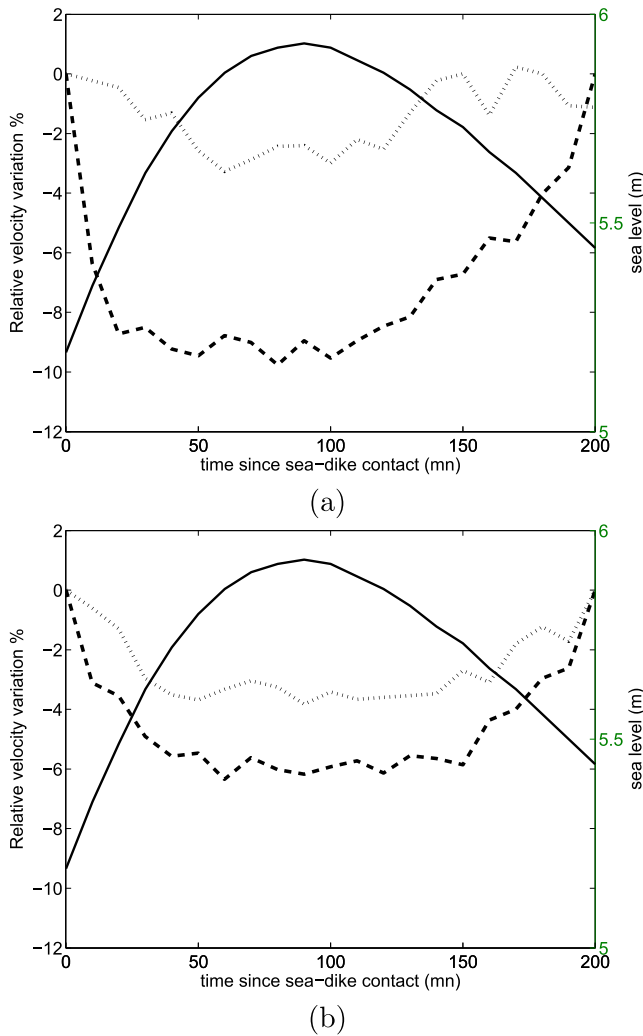


Figure 15. Relative velocity variations as a function of time, obtained from the correlation functions filtered between 21 and 39 Hz (a) and between 7 and 13 Hz (b). Full line: theoretical sea level; dashed line: variations obtained from sensors located at $x = 27$ m and $x = 42$ m; dotted line: variations obtained from sensors located at $x = 27$ m and $x = 54$ m.

should therefore not be interpreted as a change occurring inside the structure.

Figs 16(b) and (c) correspond to non-pre-whitened cross-correlations and a larger sensor spacing (9 and 12 m, respectively). Both distinct areas seen on Fig. 16(a) are visible. However, in contrast with a sensor spacing of 3 m, larger wavelengths are resolved, allowing to constrain the lower boundary of positive variations at about 25 Hz. We remind that this frequency corresponds mainly to the dike body, with a wavelength of about 13 m (see dispersion diagram in Fig. 7). We consider that a given wavelength can be properly resolved with a sensor spacing of about half its value.

In order to remove the aforementioned global variation and recover unbiased amplitudes, normalization was applied during pre-processing, either in the form of pre-whitening before cross-correlations (i.e. each record is normalized by itself, see eq. 1) or through deconvolution (which corresponds to a cross-correlation normalized only by one of the two stations in the frequency domain, see eq. 3 and Prieto *et al.* 2011). Results are shown in Figs 16(d) (pre-whitened cross-correlations) and (g) (deconvolution) for a sensor spacing of 3 m. It is seen that normalization allows to remove

most of the bias induced by source variations, allowing to detect a second area of increasing attenuation when the sea level rises. The second anomaly, located between 0 and 15 m and lower in terms of frequency, seems related to the leftmost area of decreasing velocity in Fig. 14. Similarly to non-pre-whitened cross-correlations (Fig. 16a), a sensor spacing of 3 m seems however, too small for a good resolution in frequency, in particular for the main area of increasing attenuation.

The above results confirm that both pre-whitened cross-correlations and deconvolution allow to retrieve amplitude information. As mentioned in Prieto *et al.* (2011), different studies concluded that pre-whitened cross-correlations still carry relevant amplitudes (Matzel 2007; Cupillard & Capdeville 2010; Cupillard *et al.* 2011), due to the fact that attenuation and scattering decrease the amount of coherent signal between two sensors as distance increases. It has nevertheless been suggested that the amplitude of pre-whitened cross-correlations is more affected by deviations from ideal noise conditions than amplitudes obtained from deconvolution (Snieder *et al.* 2009; Harmon *et al.* 2010; Cupillard *et al.* 2011). The comparison of Figs 16(d) and (g) show that no strong discrepancies are observed between pre-whitened correlations and deconvolutions, suggesting that conditions for the reconstruction of a realistic Green's function were met in this experiment.

Figs 16(e) and (f) show results obtained from pre-whitened cross-correlations, for sensor spacing of 9 and 12 m, respectively. It is seen that observed variations are no longer consistent with the aforementioned results in attenuation or phase velocity. For larger sensor pairs, normalizing by each station during the pre-whitening process prevents from retrieving absolute differences between the damaged and healthy sections of the dike. In contrast, cross-correlations calculated for a sensor spacing of 3 m (Fig. 16d) are in better agreement with other results, because close sensors are more likely to be located on the same area (either healthy or damaged).

Very similar results are obtained with deconvolutions calculated for sensor spacings of 9 and 12 m (Figs 16h and i). In this case, again, normalization appears to be the issue. Because deconvolution expresses in the frequency domain as a cross-correlation normalized by one of the two stations, one must be careful in the choice of the reference station. Our results, calculated as a function of location along the dike's crest, mixes deconvolution normalized alternatively by stations located either on the healthy or damaged area, leading to inconsistent results. The only way to mitigate this effect is to use small sensor pairs, as previously shown in Fig. 16(g): in this manner, normalization is performed on stations located in the same neighbourhood and unbiased temporal variations can be retrieved. This, however, comes at the cost of losing information at large depth, since only small wavelengths can be accurately measured. A similar discussion can be found in Prieto *et al.* (2011), where pre-processing normalizations and their effects on the amplitude of empirical Green's functions, are discussed in the context of sedimentary basin amplification.

We note that deconvolution results presented here were always obtained by normalizing with the leftmost sensor (see eq. 3). When using the rightmost sensor for normalization, results (not shown here) are seen to be very similar, with the exception that boundaries between distinct areas are shifted by a distance of the order of the sensor pair length. This shift is the consequence of a switching of reference between the healthy and damaged areas.

In conclusion, attenuation measurements appear to be possible in the context of sea dike passive monitoring. In this experiment, areas of increasing attenuation were found to be consistent with areas of decreasing surface wave phase velocity when the sea level rises.

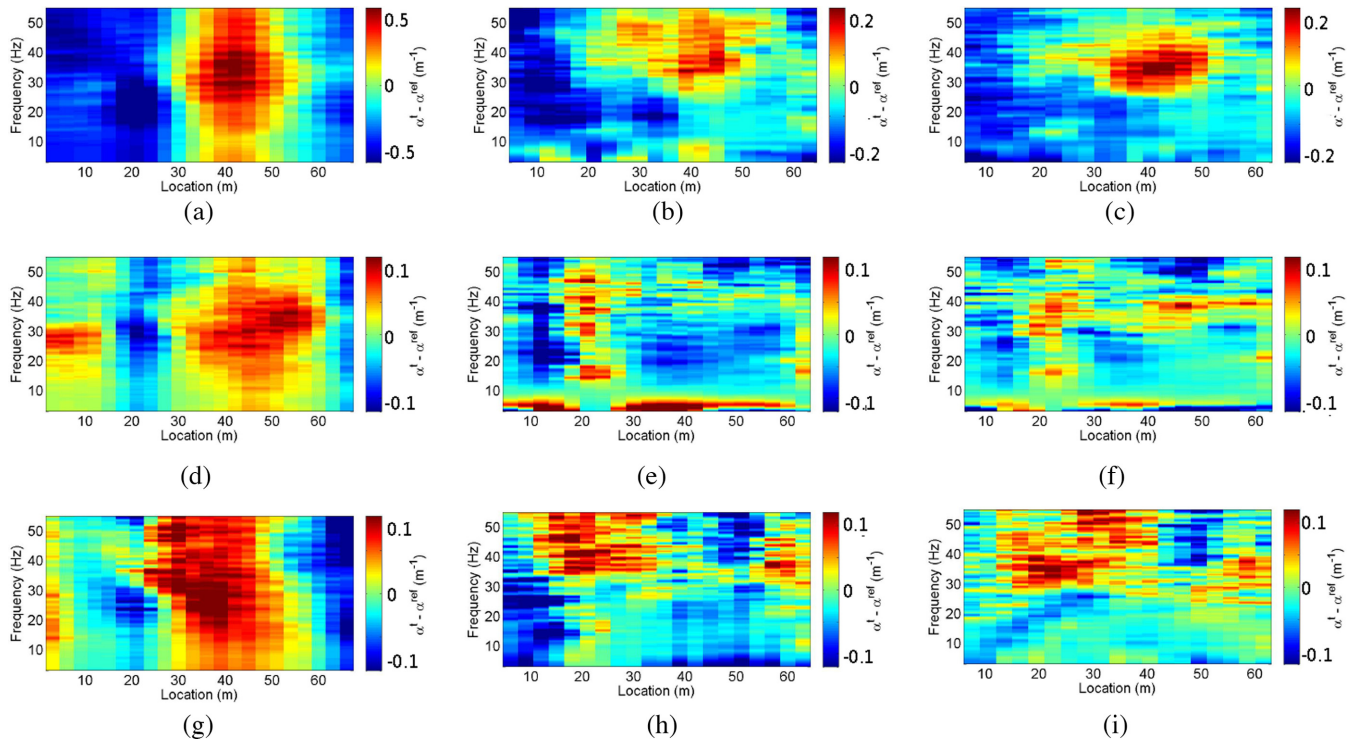


Figure 16. Attenuation variations obtained with non-whitened cross-correlation (a–c), with pre-whitened cross-correlation (d–f) and deconvolution (g–i), for three different sensor spacings: 3 m (a, d and g), 9 m (b, e and h) and 12 m (c, f and i).

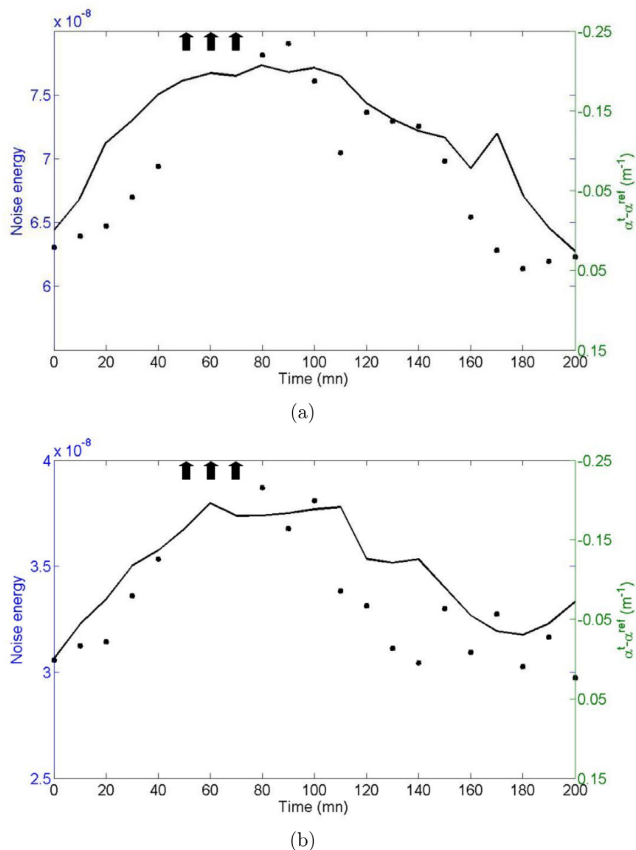


Figure 17. Variations of noise energy as a function of time, smoothed with a running average of three points (the black dots), compared with attenuation variations calculated for a sensor pair centred at $x = 6$ m, for two bandwidths: (a) 10–20 Hz and (b) 20–45 Hz.

A discussion on the physical interpretation of this observation is given in the next section. Attenuation measurements are however, sensitive to pre-processing. Different approaches have been proposed, each with specific advantages and drawbacks. In summary, non-pre-whitened cross-correlation allow for larger wavelengths to be resolved, but at the cost of not removing global effects induced by sources variations. In contrast, pre-normalization (either with pre-whitening or deconvolution) allows to remove this effect, but requires that individual sensor pairs are located in homogeneous sections of the structure.

4.3 Mechanical interpretation

Temporal variations calculated for velocity and attenuation (Figs 14 and 16) present locally an evolution between the reference time and high tide. We interpret these results as a consequence of the penetration and retreat of water within the dike, due to the presence of cracks in the masonry wall and on-going erosion of the sandy clay within the structure. This interpretation is consistent with the observation of a water leak through an aperture at the base of the masonry wall when the sea retreats.

From the mechanical standpoint, the following mechanisms can be proposed. Shear velocity is a function of shear modulus and density. The infiltration of water is expected to induce an increase of pore-water pressure and a decreasing of effective stress σ . The relationship is well established between σ and the shear modulus μ and implies the decrease of μ as σ decreases (Santamarina *et al.* 2001). Concomitantly, the density of sandy clay is likely to increase as the material gets wetter. These two effects result in lower surface wave velocity, mainly governed by the S -wave velocity. Johnston & Toksöz (1980) presented a large number of laboratory measurements that demonstrated the decrease of shear wave velocity as saturation increases.

On the other hand, friction on cracks and grain boundaries is expected to increase with saturation, due to the fact that sliding is favoured by the presence of water, leading to a decreasing of the shear wave quality factor (Johnston *et al.* 1979; Toksöz *et al.* 1979). While the quality factor of surface waves is a function of both P - and S -wave velocity and quality factors (Anderson *et al.* 1965), it was shown that the influence of compressional parameters is negligible for large V_p/V_s ratio (Xia *et al.* 2002), which is expected in the case of wet soil. As a consequence of the decrease of both V_s and Q_s with saturation, the surface wave attenuation coefficient α is expected to increase when water penetrates the body of the dike (see eq. 8).

5 CONCLUSION

Our field experiment demonstrates that the cross-correlation or deconvolution of seismic noise obtained from a linear array of sensors installed on the crest of a sea dike makes it possible to reconstruct surface waves propagating along the array. The analysis shows that 10-min records are sufficient to obtain stable waveforms in a frequency band suitable for monitoring both the dike body and its substratum, as long as the structure is in contact with sea waves. The recording time required was short enough to allow monitoring the sea dike in response to water level changes.

The empirical Green's functions calculated were used to perform both phase delay and spectral ratio measurements, in order to obtain the temporal variations of surface wave velocity and attenuation coefficient. Localized variations were observed on the velocity and attenuation measurements. These variations were interpreted as the consequence of water infiltration within the dike body.

We proposed a new approach based on the spectral amplitude ratio which complements the velocity variation measurements classically used in passive seismic monitoring studies. In addition, this method does not require the application of frequency filters on the time-domain correlation functions, and it gives a more straightforward relationship between measured variations and frequency, and therefore between measured variations and depth. Nevertheless, more work, beyond the scope of this paper, is required in order to fully understand the effects of spectral normalization in the amplitude retrieval of the empirical Green's functions.

The methods proposed here are potentially capable of quickly detecting existing internal defects inside coastal defences in contact with the sea. Further methodological developments may include a quantitative numerical study of the relationship between sensor spacing and the largest resolved wavelength as well as the inversion of measured variations as a function of depth. In addition, the deployment of long-term monitoring experiments would allow observing seasonal variations undergone by coastal defences, and detecting finer variations (≤ 1 per cent) associated with progressive long-term internal erosion processes, providing day-long or even week-long noise records for the calculation of empirical Green's functions.

ACKNOWLEDGEMENTS

We thank the french municipalities of Les Moutiers-en-Retz and Bouin for their support in the production of this work. We are grateful to both the reviewers and editor for their constructive and helpful remarks.

REFERENCES

- Anderson, D.L., Ben-Menahem, A. & Archambeau, C.B., 1965. Attenuation of seismic energy in the upper mantle, *J. geophys. Res.*, **70**(6), 1441–1448.
- Beck, Y.-L., Khan, A.A., Cunat, P., Guidoux, C., Artières, O., Mars, J. & Fry, J.-J., 2010. Thermal monitoring of embankment dams by fiber optics, in *8th ICOLD European Club Symposium*, Innsbruck, pp. 444–448.
- Bensen, G., Ritzwoller, M., Barmin, M., Levshin, A., Lin, F., Moschetti, M., Shapiro, N. & Yang, Y., 2007. Processing seismic ambient noise data to obtain reliable broad-band surface wave dispersion measurements, *Geophys. J. Int.*, **169**(3), 1239–1260.
- Bitri, A., Grandjean, G. & Samyn, K., 2011. Surface wave interferometry by crosscorrelation and deconvolution, *First Break*, **29**(5), 83–86.
- Brenguier, F., Shapiro, N.M., Campillo, M., Ferrazzini, V., Duputel, Z., Coutant, O. & Nercessian, A., 2008. Towards forecasting volcanic eruptions using seismic noise, *Nat. Geosci.*, **1**(2), 126–130.
- Campillo, M. & Paul, A., 2003. Long-range correlations in the diffuse seismic coda, *Science*, **299**(5606), 547–549.
- Clayton, R.W. & Wiggins, R.A., 1976. Source shape estimation and deconvolution of teleseismic bodywaves, *Geophys. J. Int.*, **47**(1), 151–177.
- Colas, S., 2007. Analyse statistique et cartographique de l'érosion marine, *Dossier IFEN*, **6**, ISSN 1776–8411.
- Cupillard, P. & Capdeville, Y., 2010. On the amplitude of surface waves obtained by noise correlation and the capability to recover the attenuation: a numerical approach, *Geophys. J. Int.*, **181**(3), 1687–1700.
- Cupillard, P., Stehly, L. & Romanowicz, B., 2011. The one-bit noise correlation: a theory based on the concepts of coherent and incoherent noise, *Geophys. J. Int.*, **184**(3), 1397–1414.
- Duputel, Z., Ferrazzini, V., Brenguier, F., Shapiro, N., Campillo, M. & Nercessian, A., 2009. Real time monitoring of relative velocity changes using ambient seismic noise at the Piton de la Fournaise volcano (La Réunion) from January 2006 to June 2007, *J. Volcanol. Geotherm. Res.*, **184**(1), 164–173.
- Fargier, Y., Lopes, S.P., Fauchard, C., François, D. & Côte, P., 2012. 2D-electrical resistivity imaging for sike survey: impact of the *a priori* information management, in *Near Surface Geoscience 2012–18th European Meeting of Environmental and Engineering Geophysics*, doi:10.3997/2214-4609.20143357.
- Fontan, M., Vassail, T. & Thevenin, P., 2016. Maitrise de la vulnérabilité des ouvrages maritimes et vérification de la capacité portante sous bruit de fond, *XIVème Journées Nationales Génie Côtier - Génie Civil*, doi:10.5150/jngcgc.2016.048.
- Gouedard, P. *et al.*, 2008. Cross-correlation of random fields: mathematical approach and applications, *Geophys. Prospect.*, **56**(3), 375–393.
- Harmon, N., Rychert, C. & Gerstoft, P., 2010. Distribution of noise sources for seismic interferometry, *Geophys. J. Int.*, **183**(3), 1470–1484.
- Hisada, Y., 1995. An efficient method for computing Green's functions for a layered half-space with sources and receivers at close depths (part 2), *Bull. seism. Soc. Am.*, **85**(4), 1080–1093.
- Inazaki, T. & Sakamoto, T., 2005. Geotechnical characterization of levee by integrated geophysical surveying, in *Proceedings of the International Symposium on Dam Safety and Detection of Hidden Troubles of Dams and Dikes*, 1–3 November, Xi'an, China, 8 p. Matzel, E., 2007. Imaging seismic attenuation in the crust and upper mantle by ambient noise correlation. *Eos Trans. AGU* 88 (52), Fall Meet. Suppl., Abstract S33E–08.
- Johansson, S., 1991. Localization and quantification of water leakage in ageing embankment dams by regular temperature measurements, in *Proceedings ICOLD 17th Congress Q*, Vienna, Q65, R54, pp. 991–1005.
- Johansson, S. & Dahlin, T., 1996. Seepage monitoring in an earth embankment dam by repeated resistivity measurements, *Eur. J. Eng. Geophys.*, **1**, 229–247.
- Johnston, D.H. & Toksöz, M.N., 1980. Ultrasonic P - and S -wave attenuation in dry and saturated rocks under pressure, *J. geophys. Res.*, **85**(B2), 925–936.
- Johnston, D.H., Toksöz, M. & Timur, A., 1979. Attenuation of seismic waves in dry and saturated rocks: II. Mechanisms, *Geophysics*, **44**(4), 691–711.
- Karl, L., Fechner, T., Schevenels, M., François, S. & Degrande, G., 2011. Geotechnical characterization of a river dyke by surface waves, *Near Surf. Geophys.*, **9**(6), 515–527.

- Kennett, B., 1974. Reflections, rays, and reverberations, *Bull. seism. Soc. Am.*, **64**(6), 1685–1696.
- Lai, C.G. & Rix, G.J., 1998. Simultaneous inversion of Rayleigh phase velocity and attenuation for near-surface site characterization.
- Larose, E., Roux, P. & Campillo, M., 2007. Reconstruction of rayleigh–lamb dispersion spectrum based on noise obtained from an air-jet forcing, *J. acoust. Soc. Am.*, **122**(6), 3437–3444.
- Le Feuvre, M., Joubert, A., Leparoux, D. & Côte, P., 2015. Passive multi-channel analysis of surface waves with cross-correlations and beamforming. Application to a sea dike, *J. Appl. Geophys.*, **114**, 36–51.
- Lobkis, O.I. & Weaver, R.L., 2001. On the emergence of the Green's function in the correlations of a diffuse field, *J. acoust. Soc. Am.*, **110**(6), doi:10.1121/1.1417528.
- Mainsant, G., Larose, E., Brönnimann, C., Jongmans, D., Michoud, C. & Jaboyedoff, M., 2012. Ambient seismic noise monitoring of a clay landslide: toward failure prediction, *J. geophys. Res.*, **117**(F1), doi:10.1029/2011JF002159.
- Matzel, E., 2007. Imaging seismic attenuation in the crust and upper mantle by ambient noise correlation, in *AGU Fall Meeting Abstracts*.
- Mehta, K., Snieder, R. & Graizer, V., 2007. Extraction of near-surface properties for a lossy layered medium using the propagator matrix, *Geophys. J. Int.*, **169**(1), 271–280.
- Meier, U., Shapiro, N.M. & Brenguier, F., 2010. Detecting seasonal variations in seismic velocities within Los Angeles basin from correlations of ambient seismic noise, *Geophys. J. Int.*, **181**(2), 985–996.
- Nakata, N., Snieder, R., Kuroda, S., Ito, S., Aizawa, T. & Kunimi, T., 2013. Monitoring a building using deconvolution interferometry. I: earthquake-data analysis, *Bull. seism. Soc. Am.*, **103**(3), 1662–1678.
- Park, C.B. & Miller, R.D., 2008. Roadside Passive Multichannel Analysis of Surface Waves (MASW), *J. Environ. Eng. Geophys.*, **13**(1), 1–11.
- Planès, T., Mooney, M.A., Rittgers, J.B.R., Parekh, M.L., Behm, M. & Snieder, R., 2016. Time-lapse monitoring of internal erosion in earthen dams and levees using ambient seismic noise, *Géotechnique*, **66**(4), 301–312.
- Planès, T., Rittgers, J.B., Mooney, M.A., Kanning, W. & Draganov, D., 2017. Monitoring the tidal response of a sea levee with ambient seismic noise, *J. Appl. Geophys.*, **138**, 255–263.
- Poupinet, G., Ellsworth, W. & Frechet, J., 1984. Monitoring velocity variations in the crust using earthquake doublets: an application to the Calaveras Fault, California, *J. geophys. Res.*, **89**(B7), 5719–5731.
- Prieto, G.A., Denolle, M., Lawrence, J.F. & Beroza, G.C., 2011. On amplitude information carried by the ambient seismic field, *C. R. Geosci.*, **343**(8), 600–614.
- Rittgers, J., Revil, A., Planes, T., Mooney, M. & Koelwijin, A., 2015. 4-D imaging of seepage in earthen embankments with time-lapse inversion of self-potential data constrained by acoustic emissions localization, *Geophys. J. Int.*, **200**(2), 756–770.
- Rode, S., 2012. Le chêne ou le roseau: quelles stratégies de gestion du risque d'inondation en France?, *Eur. J. Geogr.*, doi:10.4000 / cyberge0.25299.
- Rost, S. & Thomas, C., 2002. Array seismology: methods and applications, *Rev. Geophys.*, **40**(3), 2–1-2-27.
- Roux, P., 2009. Passive seismic imaging with directive ambient noise: application to surface waves and the San Andreas Fault in Parkfield, CA, *Geophys. J. Int.*, **179**(1), 367–373.
- Sabra, K.G., Gerstoft, P., Roux, P., Kuperman, W. & Fehler, M.C., 2005. Extracting time-domain Green's function estimates from ambient seismic noise, *Geophys. Res. Lett.*, **32**(3), doi:10.1029/2004GL021862.
- Santamarina, J.C., Klein, A. & Fam, M.A., 2001. Soils and waves: particulate materials behavior, characterization and process monitoring, *J. Soils Sediments*, **1**(2), 130–130.
- Seats, K.J., Lawrence, J.F. & Prieto, G.A., 2012. Improved ambient noise correlation functions using Welch's method, *Geophys. J. Int.*, **188**(2), 513–523.
- Shapiro, N.M. & Campillo, M., 2004. Emergence of broadband Rayleigh waves from correlations of the ambient seismic noise, *Geophys. Res. Lett.*, **31**(7), L07614, doi:10.1029/2004GL019491.
- Shapiro, N.M., Campillo, M., Stehly, L. & Ritzwoller, M.H., 2005. High-resolution surface-wave tomography from ambient seismic noise, *Science*, **307**(5715), 1615–1618.
- Snieder, R., 2004. Extracting the Green's function from the correlation of coda waves: a derivation based on stationary phase, *Phys. Rev. E*, **69**(4), 046610, doi:10.1103/PhysRevE.69.046610.
- Snieder, R., 2006. The theory of coda wave interferometry, *Pure appl. Geophys.*, **163**(2–3), 455–473.
- Snieder, R. & Şafak, E., 2006. Extracting the building response using seismic interferometry: theory and application to the Millikan Library in Pasadena, California, *Bull. seism. Soc. Am.*, **96**(2), 586–598.
- Snieder, R., Grêt, A., Douma, H. & Scales, J., 2002. Coda wave interferometry for estimating nonlinear behavior in seismic velocity, *Science*, **295**(5563), 2253–2255.
- Snieder, R., Miyazawa, M., Slob, E., Vasconcelos, I. & Wapenaar, K., 2009. A comparison of strategies for seismic interferometry, *Surv. Geophys.*, **30**(4–5), 503–523.
- Stehly, L., Fry, B., Campillo, M., Shapiro, N., Guilbert, J., Boschi, L. & Giardini, D., 2009. Tomography of the Alpine region from observations of seismic ambient noise, *Geophys. J. Int.*, **178**(1), 338–350.
- Toksöz, M., Johnston, D. & Timur, A., 1979. Attenuation of seismic waves in dry and saturated rocks: I. Laboratory measurements, *Geophysics*, **44**(4), 681–690.
- Vasconcelos, I. & Snieder, R., 2007. Seismic interferometry by deconvolution: Theory and examples, in *EAGE 69th Conference and Technical Exhibition (June 2007)*, doi:10.3997/2214-4609.201401667.
- Vasconcelos, I. & Snieder, R., 2008a. Interferometry by deconvolution: part 1 — theory for acoustic waves and numerical examples, *Geophysics*, **73**(3), S115–S128.
- Vasconcelos, I. & Snieder, R., 2008b. Interferometry by deconvolution: part 2 — theory for elastic waves and application to drill-bit seismic imaging, *Geophysics*, **73**(3), S129–S141.
- Vassail, T., Fontan, M. & Thevenin, P., 2016. Un nouvel outil de cartographie des digues, *XIVème Journées Nationales Génie Côtier - Génie Civil*, pp. 459–466, Thierry VASSAIL, Maxime FONTAN, Pierre-Eric THEVENIN, Romain BAYLE Un nouvel outil de cartographie des digues, doi:10.5150/jngcgc.2016.052.
- Wapenaar, K., 2004. Retrieving the elastodynamic Green's function of an arbitrary inhomogeneous medium by cross correlation, *Phys. Rev. Lett.*, **93**(25), 254301, doi:10.1103/PhysRevLett.93.254301.
- Wapenaar, K. & Fokkema, J., 2006. Green's function representations for seismic interferometry, *Geophysics*, **71**(4), SI33–SI46.
- Wathelet, M., 2008. An improved neighborhood algorithm: parameter conditions and dynamic scaling, *Geophys. Res. Lett.*, **35**(9), doi:10.1029/2008GL033256.
- Weaver, R.L. & Lobkis, O.I., 2001. On the emergence of the Green's function in the correlations of a diffuse field, *J. acoust. Soc. Am.*, **109**(5), doi:10.1121/1.4744516.
- Weller, A., Lewis, R., Canh, T., Möller, M. & Scholz, B., 2014. Geotechnical and geophysical long-term monitoring at a levee of red river in Vietnam, *J. Environ. Eng. Geophys.*, **19**(3), 183–192.
- Woods, R.D., 1968. Screening of surface waves in soils, *J. Soil Mech. Found.*, **94**, 951–980.
- Xia, J., Miller, R.D., Park, C.B. & Tian, G., 2002. Determining Q of near-surface materials from Rayleigh waves, *J. Appl. Geophys.*, **51**(2), 121–129.